

INSERT CREATIVE NAME HERE

Author's name

Bachelorarbeit in Physik
angefertigt im Argelander-Institut für Astronomie

vorgelegt der
Mathematisch-Naturwissenschaftlichen Fakultät
der
Rheinischen Friedrich-Wilhelms-Universität
Bonn

MMM 2024

DRAFT

Ich versichere, dass ich diese Arbeit selbstständig verfasst und keine anderen als die angegebenen Quellen und Hilfsmittel benutzt sowie die Zitate kenntlich gemacht habe.

Bonn,

Datum

.....

Unterschrift

1. Gutachter: Prof. Dr. John Smith
2. Gutachterin: Prof. Dr. Anne Jones

Acknowledgements

I would like to thank ...

You should probably use \chapter* for acknowledgements at the beginning of a thesis and \chapter for the end.

DRAFT

Contents

1	Introduction	1
2	Theoretical Background	2
2.1	Clusters and groups of galaxies	2
2.1.1	The Intracluster Medium (ICM)	2
2.1.2	Emission Processes within the ICM	2
2.1.3	The β -Model of the ICM	3
2.1.4	The galaxy group NGC1550	3
2.2	eROSITA	4
2.3	Skybackground and contamination sources	4
3	Data Reduction	6
3.1	Raw photon images	6
3.2	Image filtering	6
3.3	PIB Correction	7
3.4	Absorption Correction	8
3.5	Exposure Correction	8
3.6	Wavelet filtering and Point Source Removal	9
4	Data Analysis	11
4.1	Image Inspection and galaxy distribution	11
4.2	Full Azimuthal Surface Brightness Profile	11
4.2.1	Beta Model and Residual Image	15
4.3	Sectorial Surface Brightness Analysis	15
5	Conclusion	20
A	Appendix	23
A.1	PIB Map	23
Bibliography		24
List of Figures		26

DRAFT

CHAPTER 1

Introduction

Unlike the larger and more massive galaxy clusters, galaxy groups are smaller systems with typical masses around $3 \times 10^{13} M_{\odot}$ (Schneider, 2006). Despite their relative modesty, the study of galaxy groups is fundamental to our understanding of the Universe's large-scale structure (LSS), as they likely contain a significant fraction of the total baryonic mass in the Universe (Fukugita, Hogan, and Peebles, 1998). Galaxy clusters and galaxy groups are characterized by a hot, ionized gas known as the intracluster medium (ICM) or the intragroup medium (IGM), which fills the space between the galaxies. This gas emits copious amounts of X-rays making X-ray observations an essential tool for identifying and studying these structures (Kravtsov and Borgani, 2012).

The galaxy group NGC1550, first linked to the extended X-ray source RX J0419+0225 through the ROSAT All-Sky Survey (Böhringer et al., 2000), has been the subject of extensive X-ray analysis. Observations have been conducted using various instruments, including ASCA (Kawaharada, Makishima, Takahashi, et al., 2003), XMM-Newton (Kawaharada, Makishima, Kitaguchi, et al., 2009), Chandra (Sun et al., 2003), and Suzaku (Sato et al., 2010). In this thesis, data from the *extended ROentgen Survey with an Imaging Telescope Array* (eROSITA) shall be utilized characterize the X-ray surface brightness profile of NGC1550 and compare the results with previous studies.

Following a brief overview of the theoretical background in Chapter 2, Chapter 3 will focus on reducing and correcting the data for various effects. Chapter 4 will analyze the surface brightness profile of NGC1550, including detailed assessments and a beta model fitting of the full azimuthal profile. Additionally, the analysis will compare the north, south, east, and west sectors against each other and against the full azimuthal profile. Finally, Chapter 5 will present the thesis conclusions, and Chapter ?? will offer suggestions for future improvement of the analysis.

CHAPTER 2

Theoretical Background

2.1 Clusters and groups of galaxies

Throughout the Universe, galaxies are not distributed homogeneously but are instead aggregated into massive cosmic structures known as galaxy groups or galaxy clusters. Galaxy clusters – the largest relaxed structures in the Universe – typically have masses exceeding $M \gtrsim 3 \times 10^{14} M_{\odot}$, whereas galaxy groups have masses around $M \sim 3 \times 10^{13} M_{\odot}$ (Schneider, 2006). Advancements in X-ray astronomy have demonstrated that these structures are significant sources of X-ray radiation (A. G. Cavaliere, Gurkaynak, and Tucker, 1971). This emission is well understood to originate from a hot intergalactic gas known as the intracluster medium (ICM)¹, which is characterized by temperatures in the range of 10^7 to 10^8 K and constitutes the primary baryonic component of galaxy clusters (Schneider, 2006).

2.1.1 The Intracluster Medium (ICM)

Within the deep gravitational wells of galaxy clusters, the temperatures become sufficiently high to fully ionize lighter elements and partially ionize heavier elements, resulting in the formation of a plasma. This hot, diffuse, and optically thin plasma, known as the Intracluster Medium (ICM), emits significant amounts of X-ray radiation. X-ray analysis of the ICM have enabled a wide variety of cosmological studies, including large-scale structure formation in the Universe (Kravtsov and Borgani, 2012).

2.1.2 Emission Processes within the ICM

A key principle of electrodynamics is that accelerated charges radiate energy. This radiation is referred to as bremsstrahlung or "free-free" when a free charged particle, typically an electron, is accelerated by the electric field of other charges, usually ions. In the ICM, this process predominates at temperatures above $k_B T_e \gtrsim 2$ keV, where the total emissivity at solar metallicity scales approximately as $\epsilon_{\text{ff}} \propto T_e^{0.5} n_e$, with n_e and T_e as the electron number density and temperature, respectively. At lower temperatures ($k_B T \lesssim 2$ keV), line emission becomes significant, with the emissivity being roughly

¹ sometimes also called intragroup medium (IGM) in the case of galaxy groups

described by $\epsilon \propto T_e^{-0.6} n_e$. Thus, for the low energy band 0.1 to 2.4 keV one finds $\epsilon \propto n_e^2$. (Reiprich and Pacaud, 2019).

2.1.3 The β -Model of the ICM

In the mid-70s, the current description of the intracluster medium (ICM) and its emission mechanisms was pioneered by A. Cavaliere and Fusco-Femiano, 1976. The model assumes gas and galaxies share the same gravitational potential. Given constant temperature T and velocity dispersion σ_r , the radial distributions of gas n_{gas} and galaxies ρ_{gal} follow

$$\frac{n_{\text{gas}}(r)}{n_{\text{gas}}(0)} = \left[\frac{\rho_{\text{gal}}(r)}{\rho_{\text{gal}(0)}} \right]^\beta ; \quad \beta = \frac{\mu m_p \sigma_r^2}{kT}$$

where μ is the mean molecular mass, m_p is the proton mass and k is the Boltzmann constant. Using the King approximation $\rho_{\text{gal}}(r) = \rho_{\text{gal}}(0)[1 + (r/r_c)^2]^{-3/2}$ (King, 1962) and $\epsilon \propto n_e^2$, the X-ray surface brightness S_X follows the profile

$$S_X(r) = S_X(0) \left[1 + \left(\frac{r}{r_c} \right)^2 \right]^{-3\beta+1/2} .$$

The β -model is widely used to describe cluster and group emissions, despite its assumptions often being unmet. Excess core emission, for example, is typically addressed by adding a second β -model component: $S_X^{\text{tot}} = S_{X,1} + S_{X,2}$ (Reiprich and Pacaud, 2019).

2.1.4 The galaxy group NGC1550

The galaxy group NGC1550 is located at a right ascension of 64.9066° and a declination of 2.4151° , with a low redshift of $z = 0.0123$ Reiprich and Böhringer, 2002. Although the lenticular galaxy NGC 1550 has long been observable in the optical, it was first associated with the extended X-ray source RX J0419+0225 through the ROSAT All-Sky Survey Böhringer et al., 2000. The presence of this extensive X-ray halo, along with its considerable mass ($\sim 2 \times 10^{13} M_\odot$), led to its classification as a galaxy group Kawaharada, Makishima, Takahashi, et al., 2003.

Although recent studies indicate that NGC1550 does not meet the formal criteria for a fossil group Sun et al., 2003, it shares several features with such groups. One notable characteristic is its high X-ray bolometric luminosity ($\gtrsim 4.8 \times 10^{41}$ erg), which predominantly originates from a central dominant galaxy. Fossil groups are thought to be formed when member galaxies in a regular galaxy group merge into a central dominant galaxy, and evidence for this process has been found in the metal distribution of NGC1550 Kawaharada, Makishima, Kitaguchi, et al., 2009; Sato et al., 2010. Additionally, a recent study has identified signs of AGN feedback and sloshing, suggesting a minor merger occurred around 33 million years ago Kolokythas et al., 2020. While the group appears to be relaxed overall, a slight east-west elongation in the central region has been noted by multiple researchers Kolokythas et al., 2020; Sun et al., 2003.

2.2 eROSITA

The extended ROentgen Survey with an Imaging Telescope Array (eROSITA) is a highly sensitive, wide-field X-ray telescope designed to capture deep and precise images across large areas of the sky. Mounted on the Spektrum-Roentgen-Gamma (SRG) observatory in a halo orbit around the second Lagrange Point, eROSITA operates within the 0.2 to 10.0 keV energy range. It is the first instrument to perform an all-sky imaging survey in the hard X-ray band (2.0 to 10.0 keV). In the soft X-ray band (0.5 to 2.0 keV), eROSITA boasts a sensitivity that is approximately 20 times greater than that of its predecessor, the ROSAT All-Sky Survey. eROSITA features seven identical mirror modules, known as Telescope Modules (TMs), each with 54 mirror shells in Wolter-I geometry and a 1.6-meter focal length. Five TMs (TM1, TM2, TM3, TM4, TM6) have aluminum on-chip optical light filters and are collectively referred to as TM8. The remaining two TMs (TM5, TM7), designed for low-energy spectroscopy, lack these filters and are referred to as TM9. (Predehl et al., 2021). Collectively, TM8 and TM9 are referred to as TM0.

2.3 Skybackground and contamination sources

For a thorough analysis of X-ray photons, it is essential to carefully consider both external background and internal instrumental contamination effects. The following section will provide a brief overview of the most important factors relevant to this analysis.

Cosmic X-ray Background (CXB): The Cosmic X-ray background comprises multiple sources, including diffuse, unabsorbed thermal emissions from the Local Hot Bubble, a plasma cavity surrounding the Sun, and absorbed thermal emissions from the Galactic halo (Galeazzi et al., 2006). Additionally, it includes discrete extragalactic sources, predominantly unresolved AGNs (Brandt and Hasinger, 2005). The diffuse component is more prominent in the lower energy band ~ 1 keV, while the extragalactic sources dominate at higher energies.

Non-X-ray Background (NXB): The non-X-ray background consists of two main components: highly variable soft protons flares from the solar corona and Earth's magnetosphere, which can be focused onto detectors, and energetic Galactic Cosmic Ray (GCR) primaries, which interact with the detector to produce secondary particles. While primary GCR events can be mostly discarded by onboard processing, the secondary particles deposit charge in the detector, making it challenging to distinguish them from true X-ray events. (Bulbul et al., 2020)

eROSITA light leak: Shortly after the launch of eROSITA, it was observed that CCDs lacking an on-chip filter (TM9) recorded a notably higher number of events. This was attributed to optical and ultraviolet light from the Sun entering the CCD through an unidentified gap in the detector shielding and was subsequently termed “light-leak” (Predehl et al., 2021).

N_{H} absorption: As X-rays travel to the detector, they undergo photoelectric absorption in the interstellar and intergalactic medium. The cross-section $\sigma \propto E^{-3}$ is inversely proportional to energy,

causing a bias toward harder X-rays, as they interact less. Additionally, $\sigma \propto Z^5$ making metal abundance crucial for energies $\gtrsim 0.2$ keV.

CHAPTER 3

Data Reduction

In the following section, the underlying data shall be reduced and corrected for the various effects and contamination sources explained in Section 2.3. Data from eRASSX is utilized for all TMs (1-7) using *eROSITA* pipeline processing version c010. The galaxy group NGC1550 is located in skytile 065087. In addition, the surrounding skytiles 062084, 062087, 062090, 065084, 065090, 068084, 068087, 068090 are used to encompass regions up to $\sim 3R_{200}$. The data reduction is performed with the software HEASoft version XXX and the extended Science Analysis Software System (eSASS 4DR1). Images were created using astropy.

3.1 Raw photon images

Before the data reduction process, raw photon images for all combined skytiles and TMs are presented across the following energy bands: 0.2 to 2.3 keV, 2.3 to 6.0 keV, and 6.0 to 9.0 keV. The skytiles were combined using the *eSASS* task `evtool`, with no additional parameters applied to reveal all inherent deficiencies in the raw images. The raw photon images are presented in 3.1. As observed, most cluster emission is concentrated in the lower energy band, making it the focus for detecting emission structures. In this analysis, the 0.2 to 2.3 keV energy band is used. Due to the light-leak in TM9, however, the energy range is restricted to 0.8 to 2.3 keV, while for TM8 it remains 0.2 to 2.3 keV. Hereafter, this TM-dependent energy band will be referred to as the “soft band” and the 6.0 to 9.0 keV energy range as the “hard band”.

3.2 Image filtering

Each skytile is cleaned individually using `evtool` with `pattern=15` to select all event patterns and `flag=0xc00fff30` to remove bad pixels and CCD corners. Subsequently, soft proton flares are identified and mitigated through the following process: the `flaregti` task is used to generate light curves with 20 s time bins in the energy range of 5 to 10 keV. A 3σ threshold is determined; time intervals exceeding this threshold indicate elevated count rates likely due to soft proton flares. The task `flaregti` is then rerun using this threshold to establish good-time-intervals (GTIs) excluding these

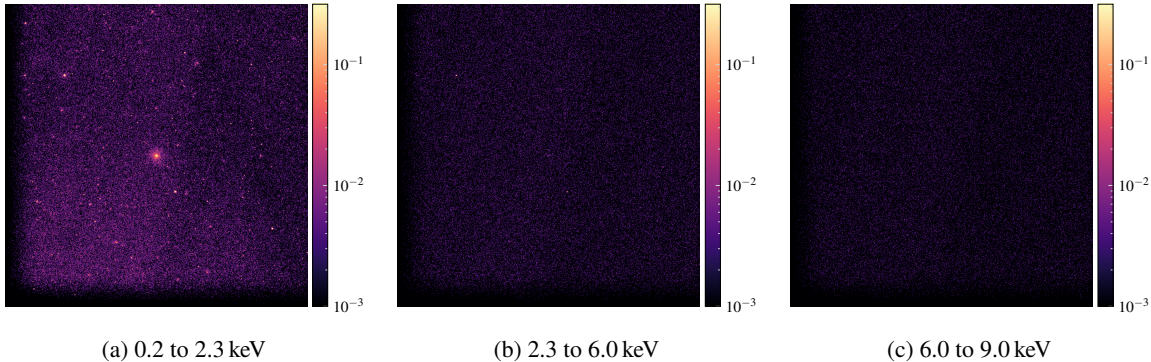


Figure 3.1: Raw photon images from TM0 of all combined skytiles centered around NGC1550, displayed in the energy bands 0.2 to 2.3 keV, 2.3 to 6.0 keV, and 6.0 to 9.0 keV, with Gaussian smoothing of 4 pixels applied. The colorbar represents (smoothed) photon counts. Most of the cluster emission is visible in the lower energy band (0.2 to 2.3 keV). A noticeable count drop on the right side of the images is evident and will be addressed through the exposure map correction detailed in Section X.

flare periods, which are applied using `evtool` with the `gti="FLAREGTI"` parameter. All SPF-filtered and cleaned skytiles are combined into a single TM0 photon image using `evtool`. Hereafter, these combined images shall be referred to as “filtered”. The `evtool` task with the `telid` parameter is also used to split the filtered photon images into individual filtered images for each TM, as needed for subsequent steps.

3.3 PIB Correction

Subtracting the particle-induced background (PIB) from the combined filtered photon image is necessary. The following approach is based on extensive studies of the *eROSITA* FWC data conducted by Dr. F. Pacaud, as utilized for example in Reiprich, Veronica, et al., 2021. The PIB is modeled for each TM using filter wheel closed (FWC) data. Due to the minimal spatial variation of the PIB, this modeling utilizes the flat exposure map created with the *eSASS* task `expmap`. Furthermore, given the negligible spectral variation, the counts H_{obs} in the hard band, where PIB counts dominate, is used to estimate the PIB contribution in the soft bands by multiplication with the ratio R of the number of FWC counts in the soft band S_{FWC} to the hard band H_{FWC} . A background map for each TM is then generated by applying this factor to the flat exposure map, normalized to 1 by dividing by the sum of all pixel values (norm. exposure map). Hence, the PIB map of a given TM is given by

$$\text{PIB map}_{\text{TM}} = H_{\text{obs}} R \cdot (\text{norm. exposure map})$$

PIB corrected image are obtained by subtracting the PIB map of each TM from the respective filtered photon image. The complete image for TM0 is obtain by co-adding all PIB corrected images. Furthermore, individual background maps are also co-added to form a complete PIB map, which can be found in Appendix A.1. Figure ?? compares the TM0 filtered image before and after PIB correction.

3.4 Absorption Correction

As discussed in Section 2.3, X-ray absorption by the ISM must be considered. The methodology outlined in Willingale et al., 2013 is followed. Additionally, scripts for the absorption correction were provided by Angie Veronica (Veronica, 2020). At higher energies ($\gtrsim 0.2$ keV), as is relevant for this analysis, absorption from metals play a significant role. Assuming solar metallicity, the hydrogen column density N_{H} can be used to trace the absorbing material. A cutout of the HI4PI all-sky survey (HI4PI Collaboration et al., 2016) is reprojected onto relevant sky tiles to create a neutral atomic hydrogen map (N_{HI} -map). Additionally, a molecular hydrogen map (N_{H_2} -map) is constructed by dividing the full sky image into 52×52 pixel cells, querying N_{H_2} values from the Swift homepage¹, and distributing these values across each cell. The total N_{Htot} -map, constructed by $N_{\text{Htot}} = N_{\text{H}} + 2N_{\text{H}_2}$, is shown in Appendix B, with N_{H} ranging from $N_{\text{Htot}, \text{min}} = 2.91 \times 10^{20} \text{ cm}^{-2}$ to $N_{\text{Htot}, \text{max}} = 1.61 \times 10^{21} \text{ cm}^{-2}$. Next, for each individual N_{H} -value in the N_{Htot} -map, the expected soft band count rates for TM1 and TM5 are simulated for the model

$$\text{apc}_{\text{LHB}} + \text{ph}_{\text{abs.}} \cdot (\text{apc}_{\text{MWH}} + \text{pow}).$$

using XSPEC² with the `fakeit` command and their respective area (ARF) and response files (RMF). Here, apc_{LHB} represents unabsorbed Local Hot Bubble emission, $\text{ph}_{\text{abs.}}$ the absorption along the line of sight, apc_{MWH} the absorbed Milky Way Halo emission, and pow the absorbed emission from unresolved point sources (e.g., AGNs). A correction factor A_{corr} is determined for each value of N_{H} by dividing the simulated count rate for the N_{H} -map median ($\overline{N_{\text{Htot}}}$) by the simulated count rate of the N_{H} of interest, hence

$$A_{\text{corr}}(N_{\text{H}}) = \frac{\text{simulated count rate}(\overline{N_{\text{Htot}}})}{\text{simulated count rate}(N_{\text{H}})}.$$

Finally, each N_{H} in the N_{Htot} -map is replaced by the corresponding correction factor A_{corr} to create an absorption correction map. Absorption correction maps are created for both TM1 and TM5, which serve as proxies for TM8 and TM9, respectively, due to their similar response files, and will be utilized in the subsequent steps.

3.5 Exposure Correction

The counts image of any given X-ray observation inherently depends on a detector's effective area and the telescope's pointing motion throughout the observation. To obtain meaningful flux units (e.g. $\text{cts} \cdot \text{arcsecond}^{-2} \text{s}^{-1}$), these effects must be considered. This is achieved by dividing the count image by an exposure map, thereby rescaling all segments of the count image to the same relative exposure (Davis, 2001). However, an exposure map must be created separately for TM8 and TM9 due to three reasons: first, TM9 uses a narrow energy band, which lowers its expected count rate;

¹ <https://www.swift.ac.uk/analysis/nhtot/index.php> (Last accessed: 25.07.2024)

² <https://heasarc.gsfc.nasa.gov/xanadu/xspec/> (Last accessed: 25.07.2024)

second, this narrower energy band necessitates a different absorption correction map; third, TM8 and TM9 have very distinct response files because of their different filter configurations. Thus, both exposure maps cannot simply be combined but must be corrected for these effects. The procedure outlined in Reiprich, Veronica, et al., 2021 will be followed. First, the exposure map of TM8 and TM9 are divided by their respective absorption correction maps to obtain an absorption-corrected exposure map ($\text{exmap}_{\text{TM8, corr}}$, $\text{exmap}_{\text{TM9, corr}}$). Second, the ratio of PIB-corrected count rates of TM8 and TM9 is used to define a correction factor

$$E_{\text{corr}} = \frac{\text{PIB corr. count rate(TM9)}}{\text{PIB corr. count rate(TM9)}}$$

The total absorption-corrected exposure map for TM0 is then given by

$$\text{exmap}_{\text{TM0, corr}} = \text{exmap}_{\text{TM8, corr}} + E_{\text{corr}} \cdot \text{exmap}_{\text{TM9, corr}}$$

Dividing the PIB-corrected TM0 image by the complete absorption-corrected exposure map leads to the final filtered, PIB-corrected, absorption-corrected and exposure-corrected image. In the following, this shall be referred to as “corrected”.

3.6 Wavelet filtering and Point Source Removal

It is necessary to remove the emission from point-like sources (e.g. AGNs) to prevent interference with the cluster emission under study. This is achieved using the wavelet filtering pipeline as described in Pacaud et al., 2006. Wavelet transformation decomposes an image $I(x, y)$ into coefficients (w_1, \dots, w_n, c_n)

$$I(x, y) = c_n(x, y) + \sum_{j=1}^n w_j(x, y).$$

Here, $c_n(x, y)$ is the smoothed image, and $w_j(x, y)$ essentially represents the contribution of a wavelet function at a scale j and position (x, y) to the total image. By retaining only the coefficients that satisfy

$$|w_j(x, y)| > k\sigma_j,$$

where σ_j is the standard deviation at scale j and k is a clipping factor, and then applying the inverse wavelet transformation, an image is obtained that includes only significant scales, i.e. those not due to noise (Starck, J.-L. and Pierre, M., 1998). The resultant image is referred to as a wavelet-filtered image. In the pipeline being used, the absorption-corrected exposure map, $\text{exmap}_{\text{TM0, corr}}$, and the raw photon image are used to account for previous data reduction and to statistically handle the Poisson noise. After wavelet filtering, a source catalogue is obtained running SExtractor (Bertin and Arnouts, 1996). This is enabled by the significant noise reduction and smoothed background achieved by wavelet filtering. The extended emission near NGC1550 is manually removed, and a cheese mask is created from the catalog and applied to $\text{exmap}_{\text{TM0, corr}}$. Unrelated emission around

IC366 is also manually added to the mask. Rerunning wavelet filtering with the cheese-masked map reduces ringing artifacts, which typically occur near steep flux gradients. Figure 3.2 compares the wavelet filtering before and after application of the cheese-mask to the exposure map.

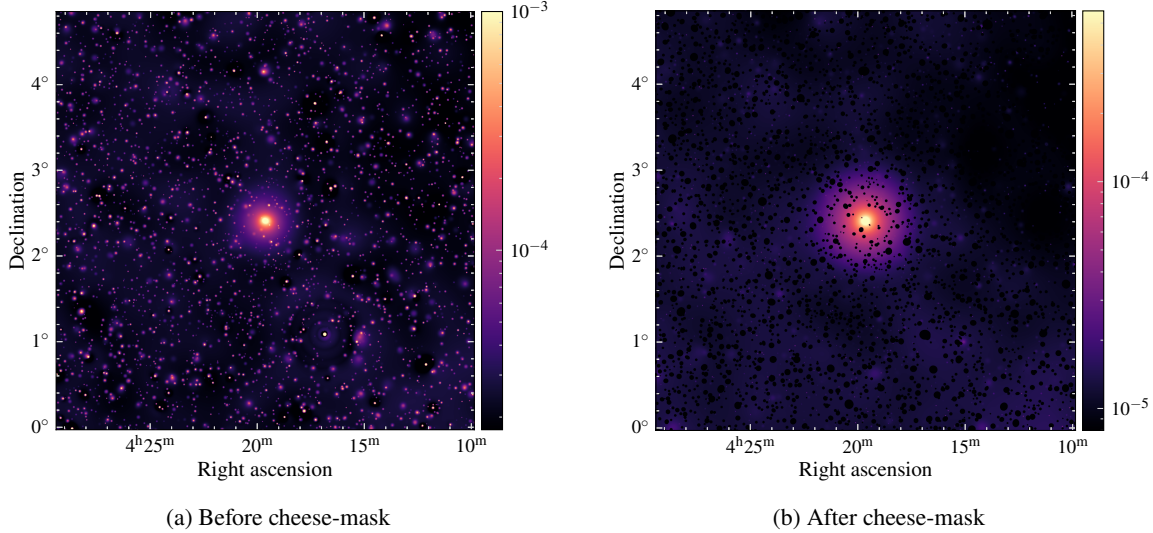


Figure 3.2: Corrected wavelet filtered image before (left) and after (right) applying the cheesemask created with **SExtractor**. The left image is normalized such that the ringing artifacts are most prominent, for example around IC366 ($\sim (4^h 16^m, 1.05^\circ)$). The cheese-masked imaged has significantly reduced ringing artifacts.

CHAPTER 4

Data Analysis

4.1 Image Inspection and galaxy distribution

A contour plot of the corrected and cheese-masked wavelet-filtered image is shown in Figure 4.2 to visualize emission beyond R_{500} more clearly. Furthermore, galaxy distribution using data from NASA/IPAC Extragalactic Database (NED) is extracted within a 1° radius of the galaxy group NGC 1550 and overlayed. There are 26 galaxies with similar redshifts $0.01 \leq z \leq 0.015$ including the galaxy NGC 1550 itself. From Figure 4.2 it is clear that the group appears spherically symmetrical and relaxed, with a distinct emission cutoff visible at R_{500} . Beyond this radius, emission becomes difficult to distinguish from the background. There is a noticeable gradient in the background emission, with a slightly lower background to the north compared to the south. The galaxy distribution is loosely clustered to the northeast, but no clear correlation with the X-ray contours is observed. Usually, this helps indicate whether excess emission along a certain direction is significant.

To highlight emission structures within R_{500} , Figure 4.1 presents a contour plot of the fully corrected image smoothed with a Gaussian kernel of 8 pixels. Within this radius, some deviations from perfect azimuthal symmetry are noticeable. A slight east-west elongation within approximately $390''$ (inner circle in the figure) can indeed be inferred as mentioned in Sectionsec:ngc1550. Beyond $390''$, features are harder to distinguish: the emission in the north, south and east appear slightly more irregular, while the emission in the west, falls more uniformly and seems slightly lower. However, it should be noted that these features are not very pronounced, even qualitatively.

4.2 Full Azimuthal Surface Brightness Profile

To more accurately identify or exclude potential deviations from spherical symmetry, surface brightness (SB) analysis will be performed. First, the emission center is estimated by constructing a $2'$ aperture around the apparent center, as given in Section X. This aperture size is chosen to capture a statistically significant number of photons without leaving the group center. The flux-weighted average coordinates of the fully corrected image within this aperture yields a right ascension of 64.909° and a declination of 2.414° and shall be referred to as the SB-center. Concentric annulli of $1'$

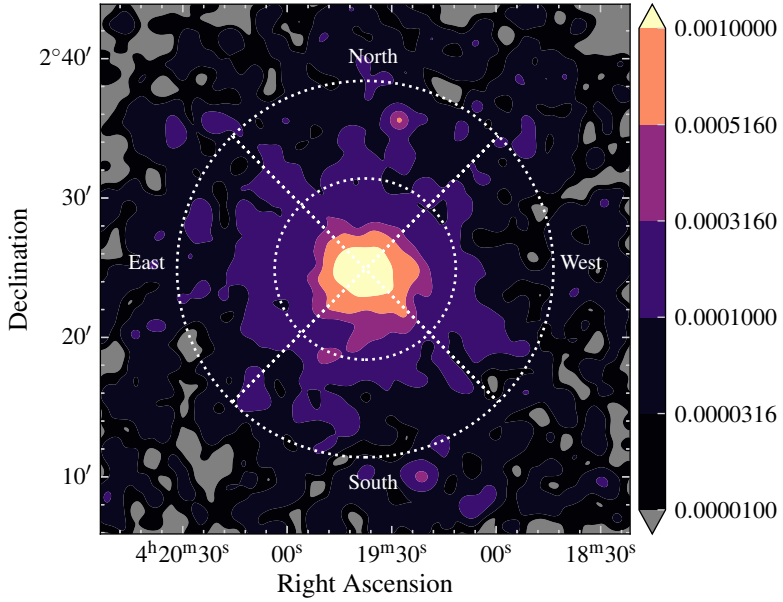


Figure 4.1: Contour plot of the fully corrected 8 pixel Gaussian smoothed image. The color bar indicates counts per second. Some deviations from azimuthal symmetry are observed within the outer circle ($\sim 810''$). The inner circle denotes a radius of $\sim 390''$. Within this region, an east-west elongation of the core is noticeable. The four wedges labeled north, south, east, and west correspond to the angular (but not radial) ranges used to extract surface brightness.

width are constructed from the SB-center up to an angular distance of $80' \sim 1.5R_{200}$. The counts C within each annulus are determined using the `funcnts` task from the `funtools` software, with a Poisson error of \sqrt{C} . The surface brightness S for each annulus is calculated by

$$S = \frac{C_{\text{filt}} - C_{\text{PIB}}}{C_{\text{expmap}} \cdot A},$$

where C denotes the counts in the filtered photon image, total PIB map, and exposure map, respectively. Errors are calculated using Gaussian error propagation. Furthermore, background estimation is performed using 10 circular regions with a $30'$ radius, each centered at a distance of $100'$ from the SB-center (Figure TODO). The average background surface brightness is evaluated for all circles combined and separately for the northern (Circles 1-5) and southern region (Circles 6-10) to account for the possibly significant background gradient. Table 4.1 lists the average background for all 3 cases. As is clear from the table, the total background level is consistent with the other two within a 1σ -Intervall. Therefore, unless otherwise specified, the total background value derived from all circles will be used for the subsequent analysis and interpretation. A β -Model is employed to

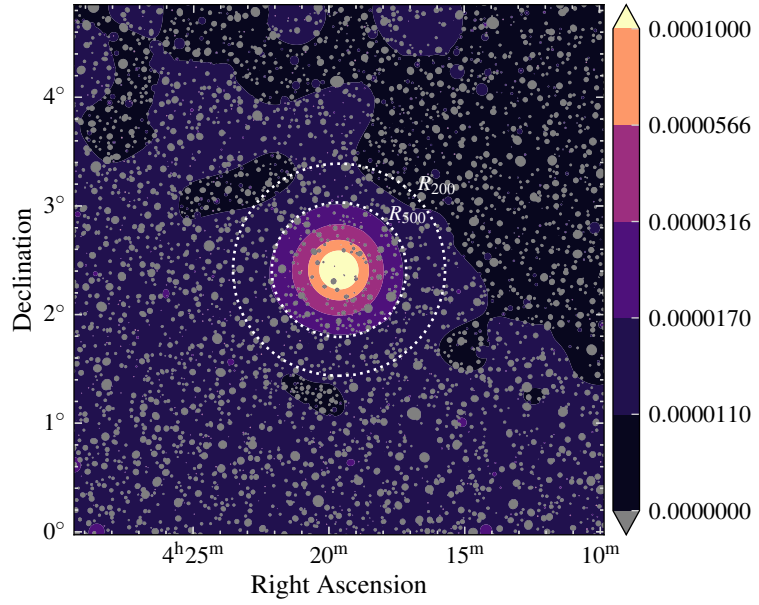


Figure 4.2: Contour plot of the corrected, cheese-masked, wavelet-filtered image with overlaid galaxy distribution (red crosses) within a 1° radius of NGC 1550. The color bar represents counts per second. The plot shows a distinct emission boundary at R_{500} , with emission beyond this radius becoming difficult to distinguish from the background. The galaxy distribution is loosely clustered to the northeast, though no clear correlation with the X-ray contours is observed.

Region	Background / $\text{cts s}^{-1} \text{arcsec}^{-2}$
North	$(1.03 \pm 0.10) \times 10^{-7}$
South	$(1.27 \pm 0.04) \times 10^{-7}$
Total	$(1.15 \pm 0.14) \times 10^{-7}$

Table 4.1: Surface brightness and associated errors for the different background regions.

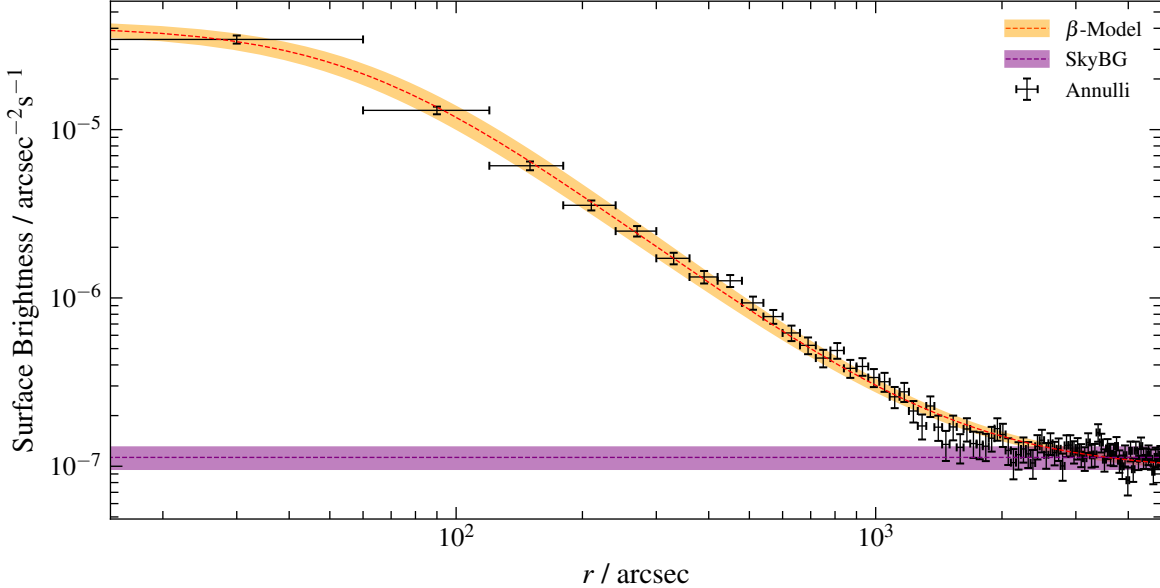


Figure 4.3: Surface Brightness within each annulus (black crosses) as a function of distance from the determined SB-center. The dashed orange line represents the best β -model fit, while the purple line indicates the observationally determined background. The shaded regions correspond to their respective 1σ intervals.

characterize the surface brightness profile, given by

$$S(r) = S_0 \left(1 + \left(\frac{r}{r_c} \right)^2 \right)^{-3\beta+0.5} + d$$

where d represents the background level. The center of each annulus is taken to be r and the corresponding surface brightness values are utilized. The optimized parameters and $\chi^2/\text{d.o.f}$ (Chi squared per degrees of freedom) are listed in Table ???. Figure 4.3 illustrates the surface brightness as a function of radial distance from the center, including both the fitted β -Model and the observationally estimated background level.

Parameter	$S_0 / \text{cts s}^{-1} \text{arcsec}^{-2}$	β	$r_c / ''$	$d / \text{cts s}^{-1} \text{arcsec}^{-2}$
	$(4.1 \pm 0.4) \times 10^{-5}$	0.478 ± 0.008	60 ± 5	$(9.3 \pm 0.4) \times 10^{-8}$
$\chi^2/\text{d. o. f}$	0.96			

Table 4.2: Fit parameters, their errors, and the reduced chi-squared value.

The beta model fit for the surface brightness profile, shown in Figure 4.3, yields $\beta = 0.478 \pm 0.008$ and core radius $r_c = (60 \pm 5)'' \sim (15 \pm 2) \text{kpc}$ with $\chi^2/\text{d.o.f.} = 0.96$. This result is consistent with previous studies: Kawaharada, Makishima, Takahashi, et al., 2003 report $\beta = 0.47$ and

$r_c \sim (16 \pm 1)$ kpc using ASCA data; Kawaharada, Makishima, Kitaguchi, et al., 2009 use a two-beta model to find $\beta = 0.50 \pm 0.05$ and $r_c \sim (20 \pm 3)$ kpc for the outer component from XMM-Newton data; Sun et al., 2003 also derive $\beta \sim 0.48$ and a slightly higher $r_c \sim 26$ kpc for the outer component using Chandra data; Reiprich and Böhringer, 2002, although, report a somewhat higher $\beta = 0.554^{+0.049}_{-0.037}$. The surface brightness profile also highlights that the group emission decreases to the background level at approximately R_{500} , as observed in Section 4.1. The observationally estimated total background, however, is approximately 24% higher than the fitted background and falls just outside the 1σ confidence interval. Although this discrepancy is not that alarming, it does indicate challenges associated with the somewhat complex background.

A two-beta model fit was not successful. This can be attributed to the limited angular resolution of the $1'$ width annuli in the core region and the degeneracy between the core radius and β . Finer annuli were attempted, but did not significantly improve the description of the surface brightness profile within the core and resulted in poor error estimation in the outskirts due to low count rates. Indeed, Kawaharada, Makishima, Kitaguchi, et al., 2009 find an inner core component of $r \sim 3$ kpc corresponding to $\sim 12''$ which is comparable to the eROSITA angular resolution $\sim 15''$.

4.2.1 Beta Model and Residual Image

Using the parameters from Table 4.2, a beta model image (Fig. 4.4) and a residual image (Fig. 4.5) are created. The beta model image is generated by distributing the one-dimensional beta model across the image. This involves computing the distance from the surface brightness center to each coordinate (x, y) in the image and then scaling the output of the beta model by the eROSITA pixel area of 16arcsec^2 . The residual image was obtained by subtracting the scaled beta model from the fully corrected image. Hence,

$$\text{res. img}(x, y) = \text{corr. img}(x, y) - S \left(\sqrt{x^2 + y^2} \right) \cdot \text{pix. area}$$

The residual image indicates that the beta model underestimates the emission around the core. This can be attributed to the absence of a second beta component, as a single beta model often inadequately describes the inner core emission, which is often higher-than-expected. Sun et al., 2003 report, however, that even a two-beta fit is not sufficient to describe the surface brightness within the central 1 kpc. Disregarding the excess emission within the core, no significant substructure or features can be noticed from the residual image.

4.3 Sectorial Surface Brightness Analysis

Thus far, the surface brightness analysis has encompassed the entire azimuthal extent of the group. By analyzing surface brightness within specific sectors and comparing them to the full azimuthal profile, elongation in certain directions can be revealed. Various authors have reported an east-west elongation at the center of NGC1550 (Sun et al., 2003, Kolokythas et al., 2020), making it particularly interesting to determine whether this elongation extends into the outer regions of the group. To investigate this, four sectorial regions (north, south, east, and west) are divided into annuli, as shown

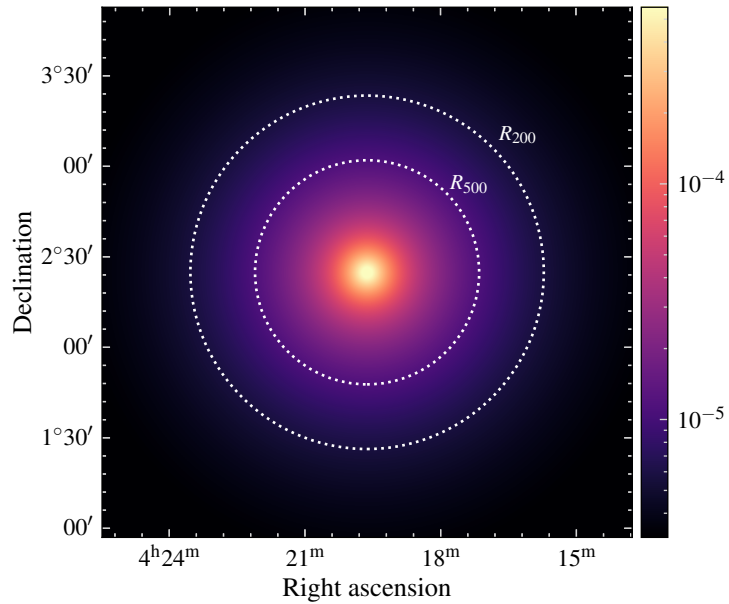


Figure 4.4: Beta model image. The colorbar represents counts per second.

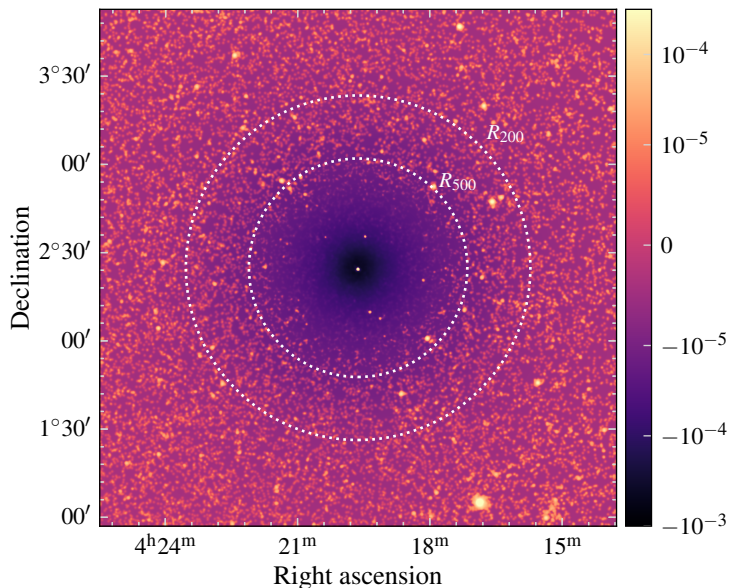


Figure 4.5: Residual image. The colorbar represents counts per second and the image has been smoothed with a Gaussian-kernel of 5 pixels. The residual image indicate that the beta model slightly overestimates the emission around the core, likely due to the inadequacy of a single beta model in capturing the core's emission.

in Figure 4.1. The center, width and extension of the annuli remain as described in Section 4.1, and surface brightness calculations and beta model fitting follow the same methodology.

Each region is initially fitted individually. Thereafter, the north and south sectors are fitted together, as are the east and west sectors. Figure 4.6(a) illustrates the comparison between the east and west profiles, as well as the north and south profiles. The top graph shows the surface brightness profiles, including the observationally determined sky background and the corresponding beta model. The lower graph displays the relative surface brightness differences of each region (SBsec) compared to the full azimuthal surface brightness profile (SBan). The error bars represent the error of the relative difference computed by Gaussian error propagation. The fit parameters for each beta model are listed in Table 4.3.

The fits are of lower quality ($\chi^2/\text{d.o.f.} \lesssim 0.8$), suggesting possible overfitting or, more likely, an overestimation of the errors as attempts using wider $2'$ annuli resulted in significantly improved $\chi^2/\text{d.o.f.} \gtrsim 0.95$ for the west, north, and combined east-west profiles, and a modest improvement for the remaining sectors. These fit parameters and $\chi^2/\text{d.o.f.}$ values are detailed in Appendix TODO. However, since the full azimuthal analysis was only performed with the smaller annuli and the resulting fit parameters are consistent across both cases, the smaller annuli will be utilized for the following comparison.

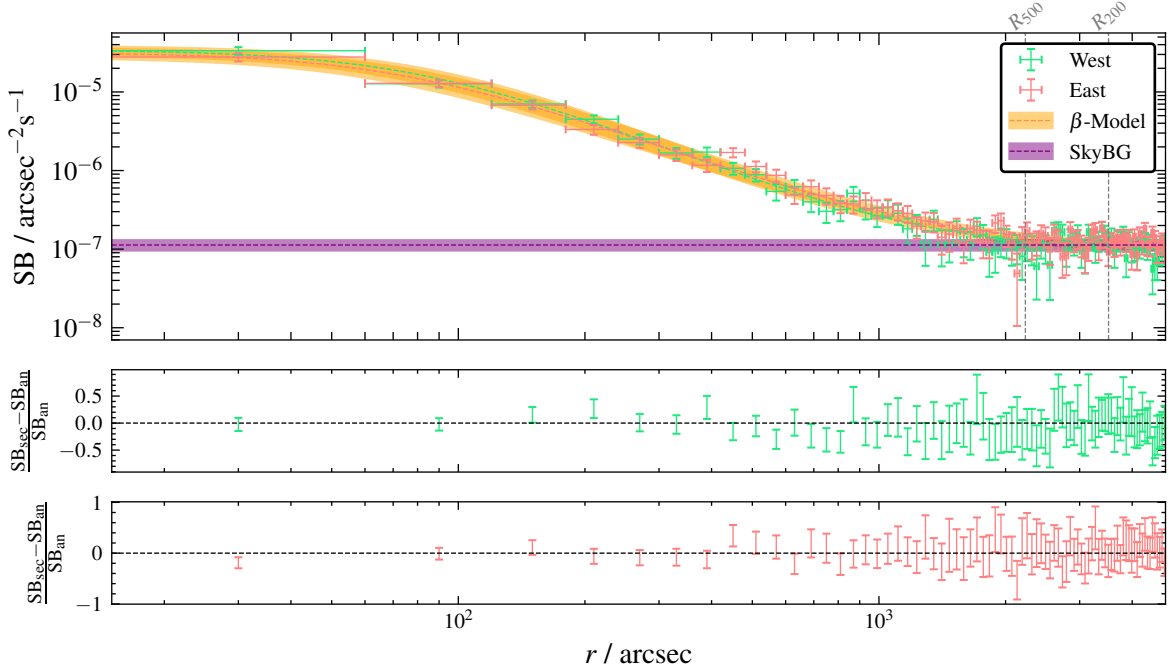
In all cases, no notable deviation from the full azimuthal profile is observed beyond $100'$. When inspecting the western region, the emission dip observed in the western region between approximately $810''$ and $390''$ —as noted in section 4.1—is noticeable in relation to the full azimuthal surface brightness plot. However, these deviations are not quantitatively significant and may be attributed to statistical fluctuations. For the northern and southern sectors, a deviation is noted at the first data point. This discrepancy is likely due to a suboptimal choice of the annuli center and is probably not physically significant. The combined east-west and north-south emissions are also compared in Figure 4.7. Here, too, no significant deviation from the full azimuthal profile is observed beyond the first data point.

It can be noticed, however, that the β -parameter and the core radius r_c are not always consistent

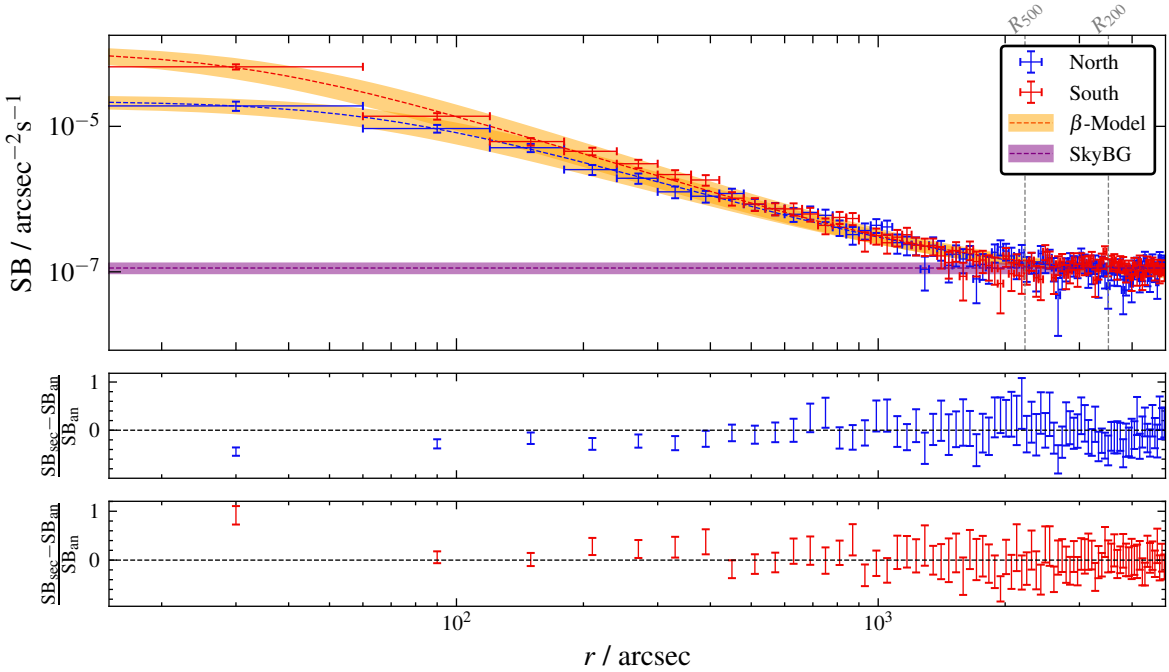
Parameter	$S_0 / \text{cts s}^{-1} \text{ arcsec}^{-2}$	β	$r_c / ''$	$d / \text{cts s}^{-1} \text{ arcsec}^{-2}$	$\chi^2/\text{d. o. f}$
East+West	$(2.88 \pm 0.27) \times 10^{-5}$	$(5.08 \pm 0.12) \times 10^{-1}$	$(8.60 \pm 0.80) \times 10^1$	$(1.02 \pm 0.05) \times 10^{-7}$	0.83
North+South	$(6.20 \pm 0.71) \times 10^{-5}$	$(4.58 \pm 0.07) \times 10^{-1}$	$(4.01 \pm 0.43) \times 10^1$	$(8.45 \pm 0.46) \times 10^{-8}$	0.71
West	$(3.42 \pm 0.42) \times 10^{-5}$	$(5.20 \pm 0.16) \times 10^{-1}$	$(8.11 \pm 0.98) \times 10^1$	$(9.63 \pm 0.60) \times 10^{-8}$	0.77
East	$(3.18 \pm 0.43) \times 10^{-5}$	$(4.87 \pm 0.15) \times 10^{-1}$	$(7.22 \pm 0.97) \times 10^1$	$(1.02 \pm 0.07) \times 10^{-7}$	0.82
North	$(2.23 \pm 0.35) \times 10^{-5}$	$(4.49 \pm 0.14) \times 10^{-1}$	$(6.6 \pm 1.1) \times 10^1$	$(7.89 \pm 0.78) \times 10^{-8}$	0.78
South	$(1.10 \pm 0.20) \times 10^{-4}$	$(4.69 \pm 0.10) \times 10^{-1}$	$(3.32 \pm 0.53) \times 10^1$	$(8.69 \pm 0.64) \times 10^{-8}$	0.86

Table 4.3: Fit parameters, their errors, and the reduced chi-squared value.

when comparing the sectors against each other and with the full azimuthal profile. For example, it is noteworthy that the core radius r_c for the combined east and west regions is more than twice as large for the north and south regions, together with $\sim 10\%$ larger β value, with the deviations being almost 3σ in both cases. (This aligns with our visual inspection in Section 4.1, which suggested that the east and particularly the west have a sharper emission drop-off compared to the north and south?). Indeed, most of the β -values and the core radii are not consistent within a 1σ interval if one compares the sectors against each other. This may be taken as an indication of the notion that no galaxy group



(a) Beta model fits for the West and East regions.



(b) Beta model fits for the North and South regions.

Figure 4.6: Beta model fits for the West-East and North-South regions. The surface brightness profiles are shown in the top graph, including the observationally determined sky background and the respective beta model. The lower graph displays the relative surface brightness differences between each region (SB_{sec}) and the azimuthal profile (SB_{an}), with error bars representing Gaussian error propagation. No significant deviation from the full azimuthal profile is observed beyond $100''$.

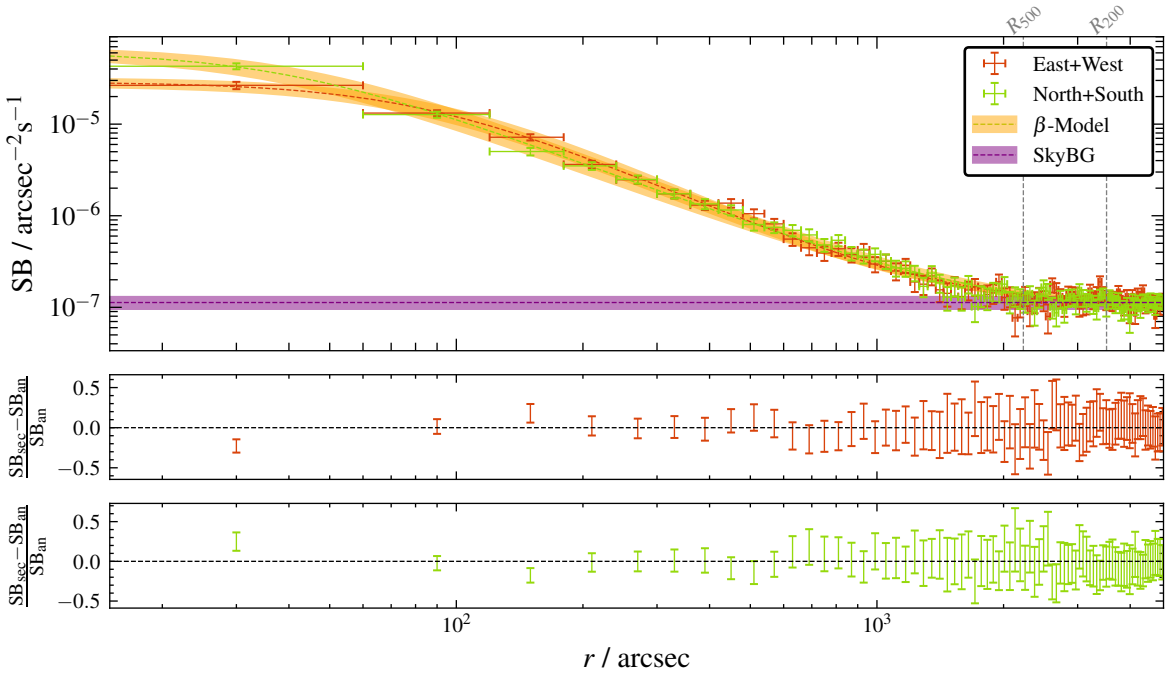


Figure 4.7: Combined beta model fits for the East+West and North+South regions. The combined surface brightness profiles show no significant deviation from the full azimuthal profile beyond the first data point.

or galaxy cluster exhibits perfect azimuthal symmetry. In-falling matter inevitably induces deviations from complete azimuthal symmetry.

CHAPTER 5

Conclusion

In the surface brightness analysis in Chapter 4, a β -model was employed to characterize the full azimuthal profile, as shown in Figure 4.3. The model fitting yielded a β -value of 0.478 ± 0.008 and a core radius of approximately $r_c = 60''$ ($\sim (15 \pm 2)$), with a reduced chi-squared value ($\chi^2/\text{d.o.f}$) of 0.96, indicating a good fit. This results was found to be consistent with the findings of various authors,

However, the analysis also highlighted a slight discrepancy between the observationally estimated background and the fitted background level, suggesting complexities in background estimation that could affect the surface brightness measurements.

A notable observation from the sectorial surface brightness analysis is the variation in the β -parameters and core radii between different sectors (north, south, east, and west). The east-west sectors exhibit a sharper emission drop-off compared to the north-south sectors, aligning with the visual elongation noted in the core region. The deviations in the β -parameters and core radii across different sectors highlight the impact of local astrophysical phenomena on the observed symmetry and radial profiles. These results align with previous studies, confirming that galaxy groups, while generally symmetrical, exhibit inherent structural variations.

The residual image analysis further supports these findings. The residuals, derived by subtracting the scaled β -model from the corrected image, indicate that the β -model slightly underestimates the emission around the core. This suggests that a single β -model did not fully capture the core's emission, necessitating consideration of multi-component models or more sophisticated modeling techniques to better describe the inner regions.

Despite the overall consistency of the surface brightness profiles within the R_{500} radius, the analysis reveals significant insights into the structural complexities of the galaxy group.

Furthermore, the background estimation process underscores the challenges associated with accurately determining background levels in astrophysical observations. The observed gradient in background emission, with a lower background in the north compared to the south, emphasizes the need for meticulous background subtraction techniques to minimize their impact on the surface brightness analysis. The consistency of the total background level with the northern and southern regions within a 1σ -interval provides confidence in the robustness of the background estimation approach, despite the noted complexities.

Chapter 5 Conclusion

Future work could focus on utilizing better modeling techniques to describe the surface brightness profile. A successful two-beta-model fit can be possible by for example fixing the core radii, utilizing more data from the inner region and utilizing more refined techniques such as convolving the beta model with the eROSITA point spread function.

Appendix

APPENDIX A

Appendix

A.1 PIB Map

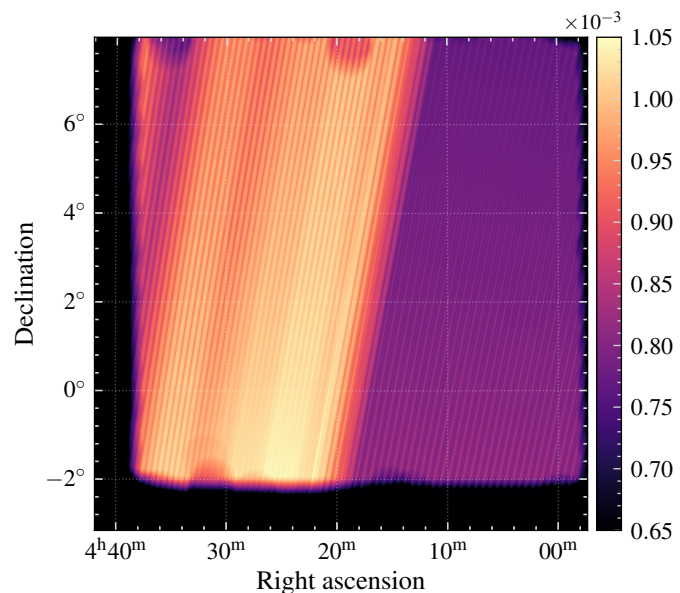


Figure A.1: PIB map created by co-adding individual background maps for each telescope module (TM).

Bibliography

- Bertin, E. and S. Arnouts (1996), *SExtractor: Software for source extraction.*, **117** 393 (cit. on p. 9).
- Böhringer, H. et al. (2000), *The Northern ROSAT All-Sky (NORAS) Galaxy Cluster Survey. I. X-Ray Properties of Clusters Detected as Extended X-Ray Sources*, **129** 435, arXiv: [astro-ph/0003219 \[astro-ph\]](#) (cit. on pp. 1, 3).
- Brandt, W. and G. Hasinger (2005), *Deep Extragalactic X-ray Surveys*, *Annual Review of Astronomy and Astrophysics* **43** 827, First published online as a Review in Advance on June 14, 2005 (cit. on p. 4).
- Bulbul, E. et al. (2020), *Characterization of the Particle-induced Background of XMM-Newton EPIC-pn: Short- and Long-term Variability*, *The Astrophysical Journal* **891** 13, URL: <https://dx.doi.org/10.3847/1538-4357/ab698a> (cit. on p. 4).
- Cavaliere, A. and R. Fusco-Femiano (1976), *X-rays from hot plasma in clusters of galaxies.*, **49** 137 (cit. on p. 3).
- Cavaliere, A. G., H. Gurksy, and W. H. Tucker (1971), *Extragalactic X-ray Sources and Associations of Galaxies*, *Nature* **231** 437, ISSN: 1476-4687, URL: <https://doi.org/10.1038/231437a0> (cit. on p. 2).
- Davis, J. E. (2001), *The Formal Underpinnings of the Response Functions Used in X-Ray Spectral Analysis*, *The Astrophysical Journal* **548** 1010, © 2001. All rights reserved. Printed in U.S.A. (cit. on p. 8).
- Fukugita, M., C. J. Hogan, and P. J. E. Peebles (1998), *The Cosmic Baryon Budget*, **503** 518, arXiv: [astro-ph/9712020 \[astro-ph\]](#) (cit. on p. 1).
- Galeazzi, M., A. Gupta, K. Covey, and E. Ursino (2006), *XMM-Newton observations of the diffuse X-ray background*, Department of Physics, University of Miami (cit. on p. 4).
- HI4PI Collaboration et al. (2016), *HI4PI: A full-sky HI survey based on EBHIS and GASS*, *Astronomy & Astrophysics* **594** A116, URL: <https://ui.adsabs.harvard.edu/abs/2016A&A...594A.116H> (cit. on p. 8).
- Kawaharada, M., K. Makishima, T. Kitaguchi, et al. (2009), *A GALAXY MERGER SCENARIO FOR THE NGC 1550 GALAXY FROM METAL DISTRIBUTIONS IN THE X-RAY EMITTING PLASMA*, *The Astrophysical Journal* **691** 971, URL: <https://dx.doi.org/10.1088/0004-637X/691/2/971> (cit. on pp. 1, 3, 15).
- Kawaharada, M., K. Makishima, I. Takahashi, et al. (2003), *A New Candidate for the Dark Group of Galaxies, RX J0419+0225*, **55** 573 (cit. on pp. 1, 3, 14).
- King, I. (1962), *The structure of star clusters. I. an empirical density law*, **67** 471 (cit. on p. 3).

Bibliography

- Kolokythas, K. et al. (2020), *Evidence of AGN feedback and sloshing in the X-ray luminous NGC 1550 galaxy group*, Monthly Notices of the Royal Astronomical Society **496** 1471, ISSN: 1365-2966, URL: <http://dx.doi.org/10.1093/mnras/staa1506> (cit. on pp. 3, 15).
- Kravtsov, A. V. and S. Borgani (2012), *Formation of Galaxy Clusters*, Annual Review of Astronomy and Astrophysics **50** 353, ISSN: 0066-4146, eprint: <https://www.annualreviews.org/doi/pdf/10.1146/annurev-astro-081811-125502>, URL: <https://www.annualreviews.org/doi/10.1146/annurev-astro-081811-125502> (cit. on pp. 1, 2).
- Pacaud, F. et al. (2006), *The XMM Large-Scale Structure survey: the X-ray pipeline and survey selection function*, Monthly Notices of the Royal Astronomical Society **372** 578, ISSN: 0035-8711, eprint: <https://academic.oup.com/mnras/article-pdf/372/2/578/2937517/mnras0372-0578.pdf>, URL: <https://doi.org/10.1111/j.1365-2966.2006.10881.x> (cit. on p. 9).
- Predehl, P. et al. (2021), *First science highlights from SRG/eROSITA: The eROSITA X-ray telescope on SRG*, A&A **647** A1 (cit. on p. 4).
- Reiprich, T. H., A. Veronica, et al. (2021), *The Abell 3391/95 galaxy cluster system: A 15 Mpc intergalactic medium emission filament, a warm gas bridge, infalling matter clumps, and (re-) accelerated plasma discovered by combining SRG/eROSITA data with ASKAP/EMU and DECam data*, AandA **647** A2, URL: <https://doi.org/10.1051/0004-6361/202039590> (cit. on pp. 7, 9).
- Reiprich, T. H. and H. Böhringer (2002), *The Mass Function of an X-Ray Flux-limited Sample of Galaxy Clusters*, The Astrophysical Journal **567** 716, URL: <https://dx.doi.org/10.1086/338753> (cit. on pp. 3, 15).
- Reiprich, T. H. and F. Pacaud (2019), *Multiwavelength Observations of Galaxy Clusters*, (cit. on p. 3).
- Sato, K. et al. (2010), *Metallicity of the Fossil Group NGC 1550 Observed with Suzaku*, Publ. Astron. Soc. Jap. **62** 1445, arXiv: [1009.4173 \[astro-ph.CO\]](1009.4173) (cit. on pp. 1, 3).
- Schneider, P. (2006), *Extragalactic Astronomy and Cosmology: An Introduction*, Second Edition, Springer-Verlag Berlin Heidelberg 2006, ISBN: 978-3-642-54082-0 (cit. on pp. 1, 2).
- Starck, J.-L. and Pierre, M. (1998), *Structure detection in low intensity X-ray images*, Astron. Astrophys. Suppl. Ser. **128** 397, URL: <https://doi.org/10.1051/aas:1998150> (cit. on p. 9).
- Sun, M. et al. (2003), *Chandra Observations of the NGC 1550 Galaxy Group: Implication for the Temperature and Entropy Profiles of 1 keV Galaxy Groups*, The Astrophysical Journal **598** 250, URL: <https://dx.doi.org/10.1086/378887> (cit. on pp. 1, 3, 15).
- Veronica, A. (2020), *X-ray Studies of the Interacting Galaxy Cluster System Abell 3391 and Abell 3395 Using eROSITA and XMM-Newton*, Masterthesis in Astrophysics, MA thesis: Argelander-Institut für Astronomie, Mathematisch-Naturwissenschaftliche Fakultät der Rheinischen Friedrich-Wilhelms-Universität Bonn (cit. on p. 8).
- Willingale, R., R. L. C. Starling, A. P. Beardmore, N. R. Tanvir, and P. T. O'Brien (2013), *Calibration of X-ray absorption in our Galaxy*, **431** 394, arXiv: [1303.0843 \[astro-ph.HE\]](1303.0843) (cit. on p. 8).

List of Figures

3.1	Raw photon images from TM0 of all combined skytiles centered around NGC1550, displayed in the energy bands 0.2 to 2.3 keV, 2.3 to 6.0 keV, and 6.0 to 9.0 keV, with Gaussian smoothing of 4 pixels applied. The colorbar represents (smoothed) photon counts. Most of the cluster emission is visible in the lower energy band (0.2 to 2.3 keV). A noticeable count drop on the right side of the images is evident and will be addressed through the exposure map correction detailed in Section X.	7
3.2	Corrected wavelet filtered image before (left) and after (right) applying the cheesemask created with SExtractor. The left image is normalized such that the ringing artifacts are most prominent, for example around IC366 ($\sim 4^{\text{h}}16^{\text{m}}, 1.05^{\circ}$). The cheese-masked imaged has significantly reduced ringing artifacts.	10
4.1	Contour plot of the fully corrected 8 pixel Gaussian smoothed image. The color bar indicates counts per second. Some deviations from azimuthal symmetry are observed within the outer circle ($\sim 810''$). The inner circle denotes a radius of $\sim 390''$. Within this region, an east-west elongation of the core is noticeable. The four wedges labeled north, south, east, and west correspond to the angular (but not radial) ranges used to extract surface brightness.	12
4.2	Contour plot of the corrected, cheese-masked, wavelet-filtered image with overlaid galaxy distribution (red crosses) within a 1° radius of NGC 1550. The color bar represents counts per second. The plot shows a distinct emission boundary at R_{500} , with emission beyond this radius becoming difficult to distinguish from the background. The galaxy distribution is loosely clustered to the northeast, though no clear correlation with the X-ray contours is observed.	13
4.3	Surface Brightness within each annulus (black crosses) as a function of distance from the determined SB-center. The dashed orange line represents the best β -model fit, while the purple line indicates the observationally determined background. The shaded regions correspond to their respective 1σ intervals.	14
4.4	Beta model image. The colorbar represents counts per second.	16
4.5	Residual image. The colorbar represents counts per second and the image has been smoothed with a Gaussian-kernel of 5 pixels. The residual image indicate that the beta model slightly overestimates the emission around the core, likely due to the inadequacy of a single beta model in capturing the core's emission.	16

List of Figures

4.6	Beta model fits for the West-East and North-South regions. The surface brightness profiles are shown in the top graph, including the observationally determined sky background and the respective beta model. The lower graph displays the relative surface brightness differences between each region (SB_{sec}) and the full azimuthal surface brightness profile (SB_{an}), with error bars representing Gaussian error propagation. No significant deviation from the full azimuthal profile is observed beyond $100''$	18
4.7	Combined beta model fits for the East+West and North+South regions. The combined surface brightness profiles show no significant deviation from the full azimuthal profile beyond the first data point.	19
A.1	PIB map created by co-adding individual background maps for each telescope module (TM).	23

List of Tables

4.1	Surface brightness and associated errors for the different background regions.	13
4.2	Fit parameters, their errors, and the reduced chi-squared value.	14
4.3	Fit parameters, their errors, and the reduced chi-squared value.	17